Two-dimensional guided $CuCrSe_2$ synthesis by spatially confined CVD and its application in neuromorphic devices

Abstract: Two-dimensional (2D) ferroelectric materials have been widely applied due to their stable ferroelectric polarization and unique physical and chemical properties. However, their ferroelectricity is constrained by their thickness and phase transition temperature. Based on the traditional chemical vapor deposition method, this paper improves and designs a spatially confined preparation technology, successfully synthesizing high-quality 2D $CuCrSe_2$ single crystals. In addition, through systematic research on the fluorophlogopite mica substrate, the orientation arrangement growth of 2D nanosheets in a specific direction was achieved. The second harmonic generation and piezoelectric response force microscopy confirmed its non-centrosymmetric structure and intrinsic ferroelectric polarization, and its ferroelectric phase transition temperature was measured to be as high as 780 K. Moreover, the horizontal and vertical memristors exhibited significant hysteresis windows and successfully simulated the basic behavior of biological synapses. Given the excellent temperature-dependent multistage conductance states and nanosecond-level fast response of the $CuCrSe_2$ synaptic device, we constructed a multi-layer CNN network to monitor the bearing conditions near rocket launches, highlighting its potential for practical applications in complex high-temperature environments.
Key words: Two-dimensional ferroelectricity; guided epitaxy; artificial synapse; neuromorphic computing

1. Introduction

Moore's Law states that the number of transistors that can be accommodated on a chip doubles every 18-24 months, and the performance also improves accordingly. However, the size of transistors has approached the physical limit, making it extremely difficult to continue increasing the density of transistors. In traditional Von Neumann architecture computers, the processing unit and the storage unit are separate entities[1-4]. In this architecture, data is retrieved from the memory storage and then sent to the processing unit for calculation. After processing, the results are sent back to the memory unit for storage. This back-and-forth movement of data increases energy consumption, processing time, and device temperature[5]. In nature, the human brain is the most powerful information processor, possessing highly parallel and efficient neural networks. Drawing inspiration from this architecture, optoelectronic synapse devices have attracted widespread attention due to their ability to simultaneously process and store data, making them an important component of the upcoming era of neuromorphic computing systems[6]. Therefore, the development of artificial synapse devices with biological synapse functions is of great significance for breaking through the "memory wall" and "power consumption wall" bottlenecks of the Von Neumann architecture.

Ferroelectric materials possess stable spontaneous polarization and their polarization direction can be reversed by an external electric field, and they have shown

extensive application prospects in various optoelectronic devices such as sensors, transducers, and non-volatile memory[7-11]. Although ferroelectricity has been verified in traditional three-dimensional (3D) ABO_3-type perovskites (such as $BaTiO_3$, $PbTiO_3$ and $BiFeO_3$), when these bulk materials are reduced to 2D films, that is, when their thickness reaches the nanometer scale, due to the influence of depolarization fields, ferroelectricity becomes weak or even disappears, which greatly limits its application in micro-nano electronic devices[12]. In contrast, 2D ferroelectric single crystals exhibit unique advantages due to their own layered structure and relatively weak interlayer van der Waals forces. Even when 2D ferroelectric materials are in a single layer or a few layers of thickness, their ferroelectricity remains stable, and their high carrier mobility, good mechanical flexibility, and optical transparency provide a good material foundation for the development of high-performance neuromorphic devices[13]. A few 2D ferroelectric materials have been experimentally verified (such as $CuInP_2S_6$, In_2Se_3, $CuCrS_2$), but most of them are prepared by mechanical exfoliation, which usually leads to uneven thickness, lateral dimensions, and shape, as well as poor controllability, and is not suitable for future large-scale integration[14-16]. Therefore, exploring and preparing high-quality 2D ferroelectric materials has become the primary task in the field of neuromorphic computing in the post-Moore era.

The AMX_2 (where A = Au, Ag, Cu; M = Cr; X = S, Se, Te) ternary compounds possess a typical non-layered structure and are a novel type of multiferroic materials (with both ferroelectricity and antiferromagnetism)[17-20]. Due to the different positions occupied by the monovalent metal A atoms between the MX_2 layers, the non-centrosymmetric structure of AMX_2 emerges. This special layered structure enables AMX_2 materials to exhibit ferroelectricity in both the in-plane (IP) and out-of-plane (OOP) directions[21]. Recently, Zhou et al. successively synthesized 2D $CuCrS_2$, $CuCrSe_2$, and $AgCrS_2$ nanosheets, and observed their interlocked IP and OOP ferroelectricity[16, 22-24]. In addition, the AMX_2 type materials have a relatively high Curie temperature (T_C). Experimental measurements show that the T_C of $CuCrS_2$ reaches 700 K, the T_C of $CuCrSe_2$ is approximately 800 K, and the T_C of $AgCrS_2$ is 682 K[16, 22-24]. These high T_C values enable the AMX_2 type materials to maintain stable ferroelectricity even in high-temperature environments, thereby expanding their application scope.

In the application of devices based on 2D materials, grain boundaries and defects can significantly affect the performance of the devices. Single crystal materials can effectively improve the performance and consistency of semiconductor devices. Unlike complex epitaxial techniques, vapor deposition can reduce defects and enhance crystallinity, thereby improving the robustness and switching durability of ferroelectric materials. Currently, chemical vapor deposition (CVD) is the main method for growing high-quality AMX_2 materials. However, the controlled preparation of large-sized high-quality 2D $CuCrSe_2$ single crystals is still in its infancy, and related research is scarce. Moreover, guided epitaxial growth can produce 2D materials with specific orientations and sizes, thereby enabling the fabrication of high-performance and high-integration ferroelectric storage devices to meet the storage and computing requirements of large-scale device arrays. Although there have been some experimental results for guided

growth of 2D materials such as WS_2 and In_2Se_3, there are still many challenges for achieving guided and controllable preparation of 2D ferroelectric materials[25, 26]. Therefore, in-depth exploration of the physical mechanism of guided growth of 2D materials and the search for more effective growth control methods have important scientific significance and practical value.

This paper reports a spatially confined CVD method that grows oriented 2D $CuCrSe_2$ nanosheets. Using the newly discovered fluorophlogopite mica as the growth substrate, the continuous control of 2D oriented $CuCrSe_2$ from nucleation, epitaxy to quasi-film was achieved. The crystal structure was confirmed by scanning transmission electron microscopy (STEM), indicating that Cu atoms were inserted into the $CrSe_2$ interlayer. The second harmonic generation (SHG) signal confirmed the non-centrosymmetric structure of $CuCrSe_2$, and the Curie temperature was measured to be approximately 780 K. The piezoelectric response force microscopy (PFM) measurement proved the IP and OOP ferroelectricity in 2D $CuCrSe_2$. Moreover, the IP and OOP ferroelectric polarization was also verified in horizontal and vertical devices. In terms of brain-like learning, these devices exhibit basic behaviors of biological synapses such as long-term potentiation/depression (LTP/LTD), short-term memory/long-term memory (STM/LTM), and human learning-forgetting behaviors. Based on the excellent multilevel conductance states of the device, we constructed a multi-layer CNN network to monitor the bearing conditions near rocket launches. Our work has made a significant contribution to the development of artificial synapse devices based on 2D ferroelectric materials and provides a brand-new option for high-performance brain-inspired computing and neuromorphic computing.

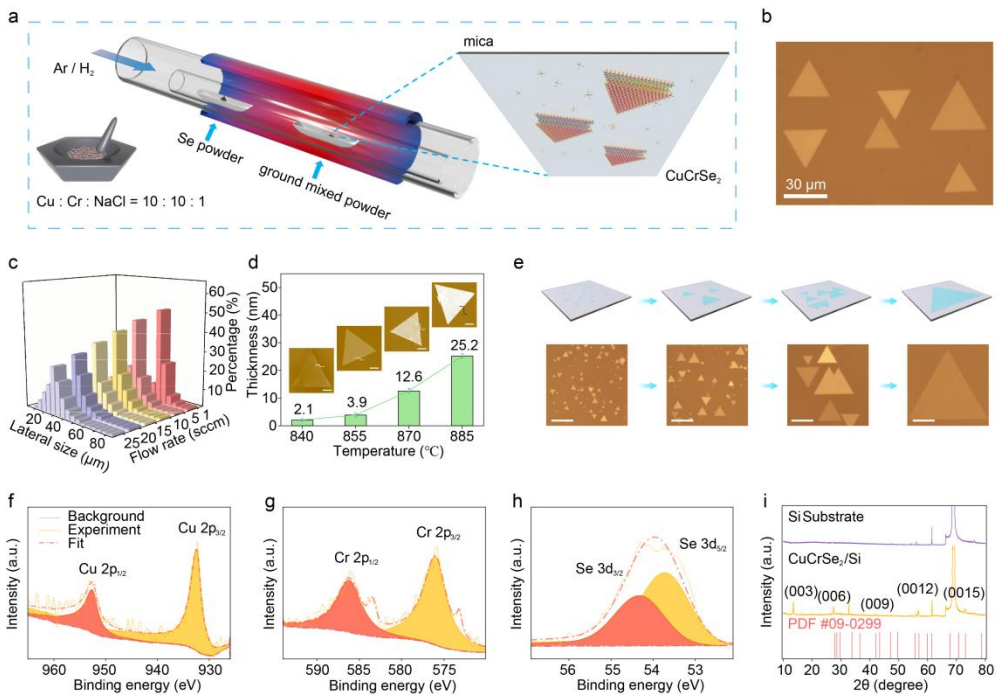

Figure 1. Directed Growth and Characterization. (a) Schematic illustration of the CVD growth process. (b) The OM image of a typical oriented-growing triangular $CuCrSe_2$ nanosheets. The statistical results of the lateral size (c) and average thickness (d) of the $CuCrSe_2$, the scale bars are

5 μm. (e) The specific growth evolution process, the scale bars are 30 μm. (f-h) XPS spectra of Cu 2p, Cr 2p, and Se 3d in $CuCrSe_2$ nanosheets, respectively. (i) XRD peaks for $CuCrSe_2$ nanosheets on the Si substrate.

2. Results and Discussion

2.1 Directed Growth and Characterization of 2D $CuCrSe_2$ Nanosheets

By improving the spatial confinement CVD technology and combining with the unique atomic structure of fluorophlogopite mica, 2D $CuCrSe_2$ nanosheet arrays with directional alignment were successfully prepared. The growth schematic is shown in Figure 1a and Figure S1. Using the newly split fluorophlogopite mica as the growth substrate, with an atomically flat, clean and chemically inert surface, and weak van der Waals interactions between the precursor and the mica surface, the precursor can nucleate on the surface and migrate with a relatively low barrier, enabling 2D $CuCrSe_2$ to be easily epitaxially grown on the mica[27]. We also attempted different substrate growths, and only irregular small and thick films were obtained on silicon wafers (Figure S2, Supplementary Information). During the growth process, the first mica provided the confined space, the second mica served as the growth substrate, and the Se vapor concentration was reasonably controlled. Firstly, the confined space reduced the Se concentration, preventing excessive Seation of the metal precursor and thus avoiding the formation of bulk by-products; secondly, the limited space stabilized the vapor pressure and effectively controlled the nucleation density, allowing $CuCrSe_2$ to grow in a large area by van der Waals epitaxy. Additionally, the introduction of sodium chloride can lower the reaction temperature and react with the non-volatile Cu and Cr metals to form evaporable metal chlorides, ensuring sufficient metal precursor supply and avoiding the formation of various by-products, which is crucial for the epitaxial growth of non-layered $CuCrSe_2$ nanosheets[28, 29]. The morphology of $CuCrSe_2$ nanosheets is controlled by the growth temperature (Figure S3, Supplementary Information), circular nanosheets were grown at 850 °C, mostly triangular at 870 °C, and hexagonal at 900 °C, mainly due to different concentrations of Cr and Se. Moreover, more evaporated Cu atoms will lead to out-of-plane growth, and the thickness of the nanosheets will increase. The crystalline quality of $CuCrSe_2$ nanosheets is affected by the gas flow rate. At low Ar/H_2 flow rates, the grown materials are regular and smooth; non-crystalline samples were grown at a 50 sccm flow rate. For more details on sample synthesis, refer to the experimental section.

The top view (left) and side view (right) of the $CuCrSe_2$ atomic structure are shown in Figure S4. Generally, the $CuCrSe_2$ crystal presents a rhombic crystal structure, with lattice constants a = b = 0.368 nm and c = 1.938 nm, belonging to the R3m space group[30]. $CuCrSe_2$ has a non-centrosymmetric and non-layered crystal structure, in which Cu atoms are inserted into the $CrSe_2$ interlayer in a 3R stacking order and occupy the same side position of the tetrahedron between two $CrSe_2$ layers. When an electric field is applied, the Cu atoms can move to the other side[31]. The non-centrosymmetric structure of $CuCrSe_2$ meets the basic requirements of ferroelectric materials.

Figure 1b shows the OM image of a typical oriented-growing triangular $CuCrSe_2$ nanosheets, confirming the uniformity and integrity of the sample surface. The statistical results of the lateral size and average thickness of the $CuCrSe_2$ nanosheets

are as follows: the lateral size (ranging from 5 μm to 80 μm) and thickness (ranging from 2 nm to 25 nm), as shown in Figure 1c and Figure 1d respectively. We used atomic force microscopy (AFM) to check the thickness of the $CuCrSe_2$ nanosheets. The inset in Figure 1d shows ultra-thin $CuCrSe_2$ with a thickness of only about 2 nm, which can be regarded as a single crystal unit cell layer due to the lattice constant c = 1.938 nm. To prepare nanosheets with larger lateral sizes, we gradually reduced the flow rate of the carrier gas Ar/H_2 and appropriately prolonged the growth time. It can be observed that the 2D oriented $CuCrSe_2$ nanosheets will gradually extend and connect from the oriented triangular arrangement to form larger triangles, and eventually connect to form the shape of a single-crystal quasi-film. The specific growth evolution process is shown in Figure 1e. The upper figure is a growth schematic diagram (including four processes: nucleation, oriented growth, epitaxial splicing, and film formation), and the lower figure is the corresponding OM photo.

We preliminarily determined the chemical composition and oxidation state of the $CuCrSe_2$ nanosheets on the mica surface. Therefore, X-ray photoelectron spectroscopy (XPS) was conducted, as shown in Figures 1f-h. The results confirmed that it was a pure phase $CuCrSe_2$, with the peaks at 952.6 eV and 932.4 eV being Cu $2p_{1/2}$ and Cu $2p_{3/2}$, respectively[32]. The peaks at 586.2 eV and 576.0 eV were Cr $2p_{1/2}$ and Cr $2p_{3/2}$, respectively. The other two peaks at 583.4 and 573.2 eV were attributed to satellite peaks[33]. The characteristic double peaks in the Se 3d region, $3d_{3/2}$ and $3d_{5/2}$, were located near 54.3 and 53.7 eV, respectively. All these XPS results were in excellent agreement with the previously reported peak positions. To further confirm the structure and phase of the $CuCrSe_2$ sample, these nanosheets were transferred onto a silicon substrate for X-ray diffraction (XRD) characterization (Figure 1i). Five main diffraction peaks corresponding to the (003), (006), (009), (0012), and (0015) crystal planes were found, all belonging to the [001] crystal plane family. This indicates that high-quality 2D $CuCrSe_2$ single crystals were synthesized.

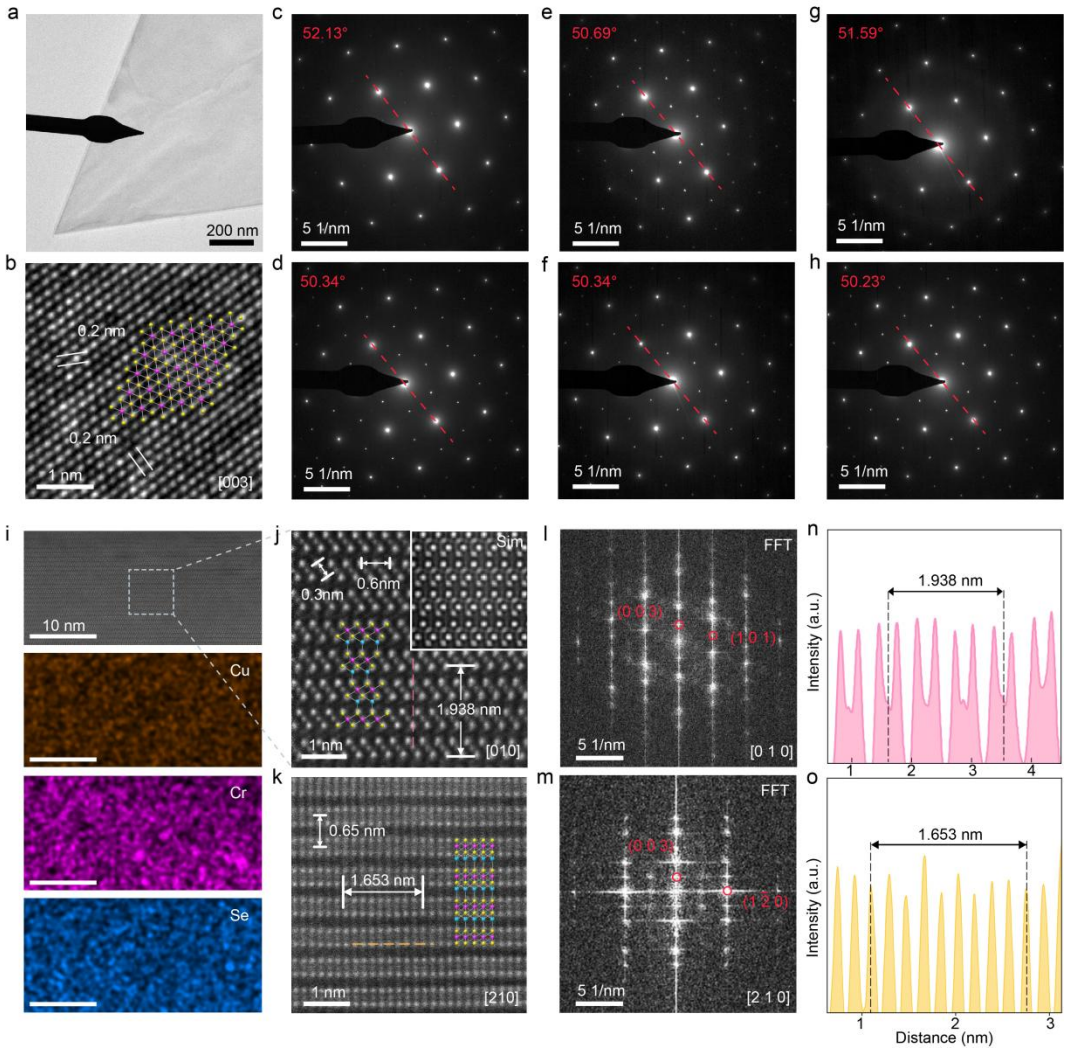

Figure 2. Atomic structure characterizations. (a) The TEM morphology image of the $CuCrSe_2$ sample. (b) The high-resolution TEM results. (c-h) The SAED patterns from six different positions. (i) The low-resolution HAADF-STEM image of the vertically cut $CuCrSe_2$ sample and the corresponding EDS element mapping images of Cu, Cr, and Se elements. Cross-section STEM image of $CuCrSe_2$ nanosheet along [010] zone axis (j) and [210] zone axis (k), inset is the simulative STEM image of $CuCrSe_2$ crystal. (l, m) The corresponding FFT diffraction spots. (n, o) Intensity profile extracted from the STEM image along the pink and orange dashed lines in (j) and (k), respectively.

The 2D oriented $CuCrSe_2$ arrays prepared in the above experiment were transferred onto a copper substrate for TEM characterization. Six triangular regions with consistent orientation were selected to observe their morphology, high-resolution, and selected area electron diffraction patterns. From the TEM morphology image of the $CuCrSe_2$ sample in Figure 2a, it can be observed that the surface of the sample is smooth and flat. The high-resolution TEM results are shown in Figure 2b, with clear atomic spots and perfect lattice periodicity indicating the synthesis of high-quality $CuCrSe_2$ single crystals, and no grain boundaries, dislocations, or defects exist. Figure S6a is a low-magnification TEM image of the sample, and it can also be observed that the triangular samples are arranged in 0° or 60° orientations. The selected area electron

diffraction images (SAED) from six different positions show that the $CuCrSe_2$ crystal exhibits six-fold rotational symmetry, and confirm that the synthesized sample is a 2D single crystal material, as shown in Figures 2c-h. The angles between the same crystal plane and the horizontal position in the SAED images are marked in the upper left corner, and the results show similar angles. The maximum deviation is only 1.9 degrees, and these negligible deviations are mainly attributed to the minor displacements or folds generated during the sample transfer process. The corresponding angle statistical results and elemental quantitative EDS spectra are shown in Figure S6b. The above results confirm that the chemically balanced $CuCrSe_2$ nanosheets have successfully achieved specific orientation growth.

Based on the cross-sectional TEM technique, we can observe the atomic arrangement of the $CuCrSe_2$ crystal more clearly. The low-resolution high-angle annular dark-field scanning transmission electron microscopy (HAADF-STEM) images of the vertically cut $CuCrSe_2$ sample and the corresponding TEM energy-dispersive X-ray spectroscopy (EDS) element mapping images (Figure 2i) indicate the uniform distribution of Cu, Cr, and Se elements. From the high-resolution cross-sectional HAADF-STEM image of the $CuCrSe_2$ nanosheets along the [010] zone axis (Figure 2j), we can clearly observe that Cu atoms are inserted into the 2D structure of the $CrSe_2$ interlayer. The structural composition of one unit cell (1.938 nm) is considered to have three atomic layers of $CrSe_2$-Cu-$CrSe_2$, and the $CrSe_2$-Cu-$CrSe_2$ layers are arranged periodically. The experimental results perfectly overlap with the corresponding simulated STEM images (Figure 2j inset). Figure 2k shows the HAADF-STEM image of the $CuCrSe_2$ nanosheets along the [210] zone axis. We can see four vertical arranged bright spots in each layer, with a layer spacing of 6.5 Å, which is one-third of the thickness of one unit cell. Due to the larger atomic number of Se atoms, brighter spots are presented. The corresponding Fast Fourier Transform (FFT) patterns are shown in Figures 2l and 2m. We also measured the unit cell thickness along the [010] and [210] zone axis directions (the pink and orange dotted lines in Figures 2j and 2k), and the results perfectly match the theoretical value of 1.938 nm (Figures 2n and 2o). In conclusion, we successfully grew high crystalline quality 2D $CuCrSe_2$ nanosheets by the salt-assisted CVD method.

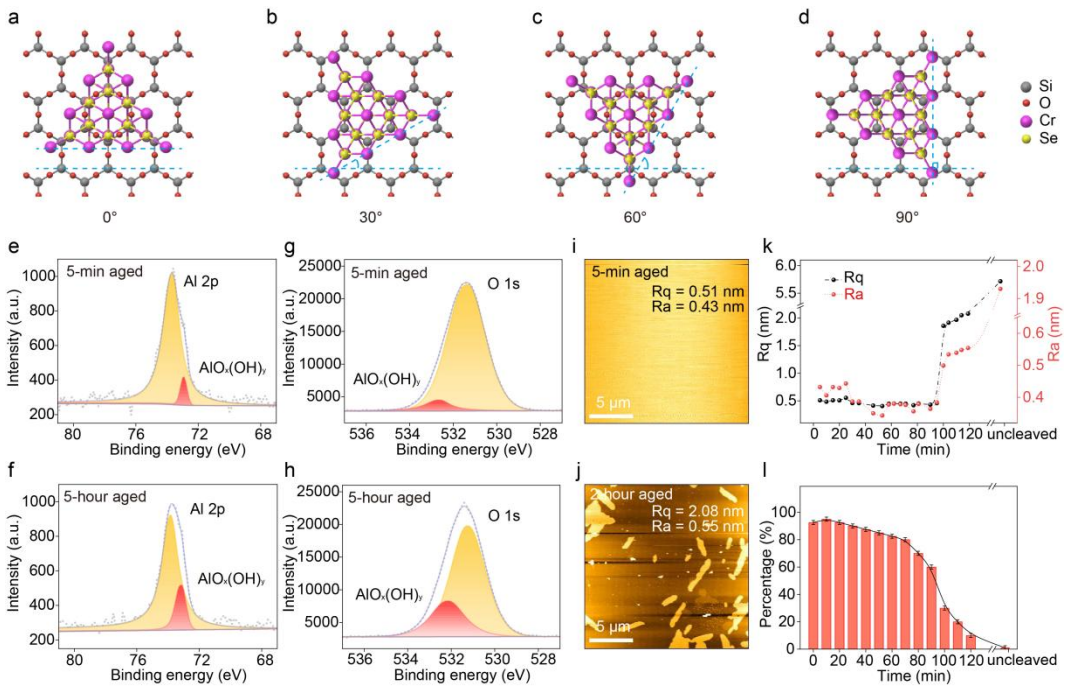

Figure 3. Exploration of the Mechanism of Directed Growth. (a-d) The atomic arrangement of $CuCrSe_2$ and fluorophlogopite mica. (e-h) XPS spectra of freshly split mica after oxidation for 5 minutes and 5 hours, respectively. (i-j) AFM surface scanning results of mica after oxidation for 5 minutes and 2 hours, respectively. (k) The surface roughness of the mica after cutting and placed for different time. (l) The relationship between the orientation rate of 2D $CuCrSe_2$ and the oxidation time of mica.

2.2 Exploration of the Mechanism of Directed Growth

Then, the orientation growth mechanism of 2D $CuCrSe_2$ was investigated to reveal its physical origin. The lattice symmetry matching relationship between the substrate and the sample is the key to assembling the nanosheets into a single-crystal film[26]. If the symmetry group of the 2D material matches the lattice symmetry of the substrate, then the 2D material can be grown with an oriented arrangement on the substrate. Therefore, choosing an appropriate substrate plays a crucial role in the epitaxial growth of $CuCrSe_2$ single crystals. The new split mica was selected as the growth substrate because its cleaved atomic surface has the same triple rotational symmetry as $CuCrSe_2$, which promotes the directional growth of $CuCrSe_2$ on the substrate into a parallel array of material units. When the alignment angle between $CuCrSe_2$ and the substrate is 0°, the $CuCrSe_2$ thin sheets reach the lowest binding energy state; at an orientation angle of 60°, the binding energy is another local minimum, slightly larger than the global minimum[26]. The atomic arrangement of $CuCrSe_2$ and mica is shown in Figures 3a-d. The guiding rate of the triangular $CuCrSe_2$ thin sheets changes with the oxidation time of mica. Therefore, XPS characterization was performed on the mica sheets placed in the air for different oxidation times after peeling to observe the elemental composition and changes on the mica surface. As shown in Figures 3e-h, additional low binding energy peaks were observed at 73 eV (Al 2p) and 532 eV (O1 s), indicating the presence of surface-enriched new substances. Previous studies have shown that exposure of the substrate to air may lead to surface hydrolysis, forming aluminum hydroxide, which

subsequently decomposes into oxygen-deficient $AlO_x(OH)_y$[25]. Therefore, attributing the shoulder peak to the exposure of the substrate to air, the formation of surface $AlO_x(OH)_y$ was observed. Comparing the test results of 5 minutes and 5 hours of oxidation, it can be seen that the longer the mica exposed to air after being split, the more obvious the new peak signals in the XPS spectrum. These results indicate that this change in the surface chemical properties of the mica seems to be unfavorable for the orientation growth of $CuCrSe_2$. Subsequently, AFM characterization was performed on the mica exposed to air for different times to observe the surface changes from another perspective. The surface roughness of the mica after cutting and placed for different time was tested, and the results are shown in Figures 3i-k. At 100 minutes of oxidation, the surface roughness of the mica suddenly increased, which may seriously affect the orientation epitaxial growth of the 2D nanosheets. The evolution process of the decline in the orientation growth guiding rate is consistent with the AFM test results. In addition, AFM surface scanning results observed the appearance of particles on the mica surface after two hours. During the mica substrate exposure process, the formation of aluminum hydroxide caused the deterioration of the substrate surface roughness, which damaged the orientation epitaxial growth of the nanosheets. During the long-term air exposure process, clusters formed on the amorphous layer. The above XPS spectral features and AFM roughness results indicate that the surface of the exposed substrate has undergone oxidation modification and formed a surface amorphous oxide layer, which has a significant impact on the material's orientation epitaxial growth.

After splitting the mica sheets and allowing them to stand for different durations (0-150 minutes), $CuCrSe_2$ growth was carried out. Figure S9 shows the optical photos of $CuCrSe_2$ on the substrate after different durations of oxidation. By comparison, it can be observed that the mica sheets that were newly split and left in the air for a longer period of time have a lower orientation rate of triangular $CuCrSe_2$ nanosheets. Figure 3l presents the relationship between the 2D $CuCrSe_2$ orientation rate and the duration of the mica sheet's placement. After 100 minutes of oxidation in the air, the orientation rate of the triangular nanosheets sharply decreased, showing a random arrangement phenomenon. Figure S10 is a statistical image of the angle between the triangular nanosheets and the lower edge of the photo, corresponding to 0 minutes, 100 minutes, and 150 minutes of substrate oxidation. The freshly peeled fluorogold mica substrate can grow only 0° or 60° oriented triangular ones; as the exposure time increases, triangular ones with other angles (30° and 90°) appear on the substrate; when the oxidation time reaches two hours, the triangular shapes on the substrate will randomly arrange and no longer follow an orientation pattern.

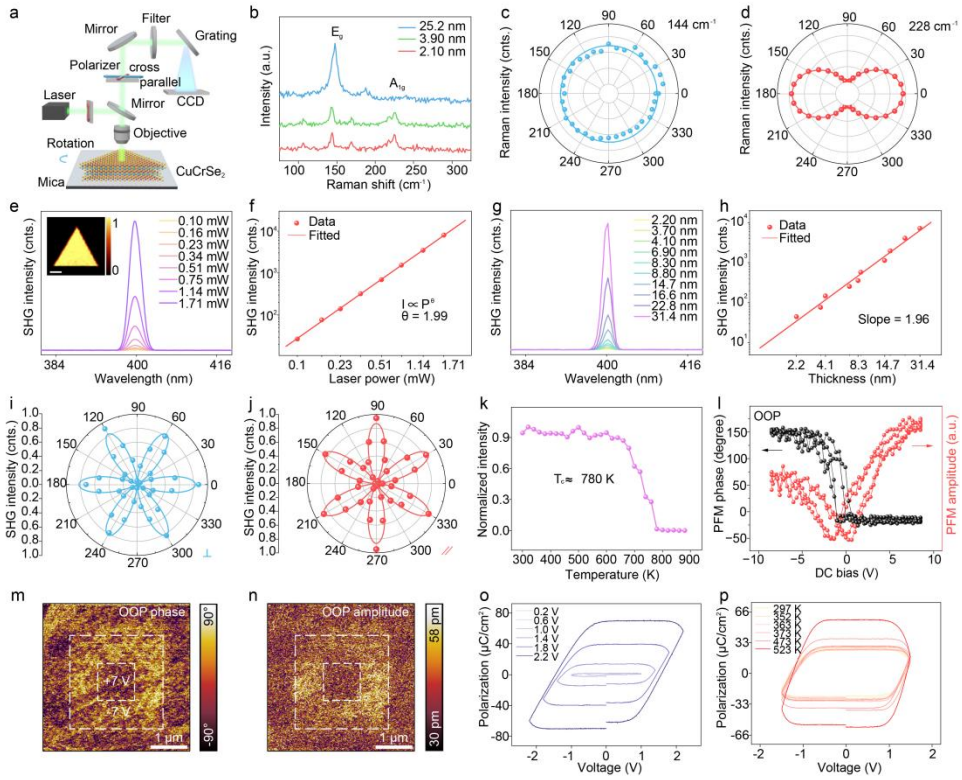

Figure 4. Second order nonlinear optical property and ferroelectric property. (a) The schematic diagram of the Raman test. (b) Thickness-dependent Raman spectra of $CuCrSe_2$ nanosheets. (c, d) The angle-resolved polarized Raman spectra at 144 cm-1 and 227 cm-1, respectively. (e) Power-dependent SHG spectra of $CuCrSe_2$ nanosheet under the excitation wavelength of 800 nm. Inset is typical SHG intensity mapping image, the scale bar is 10 μm. (f) The excitation power dependence of SHG intensity with the coefficient fitted to 1.99. (g) Thickness-dependent SHG spectra of $CuCrSe_2$ nanosheet. (h) The thickness dependence of SHG intensity with the coefficient fitted to 1.96. (i, j) Polarization angle-dependent SHG intensity under perpendicular and parallel polarization configurations, respectively. (k) Temperature-dependent normalized SHG intensity of $CuCrSe_2$ nanosheets, exhibiting an indication of ferroelectric-paraelectric phase transition. (l) OOP PFM phase hysteretic and butterfly loops of $CuCrSe_2$ nanosheet. (m) PFM OOP phase, (n) OOP amplitude images with box-in-box pattern (dashed regions) written by opposite DC bias, respectively. The P-E curves under different voltages (o) and temperatures (p), respectively.

2.3 Source and Verification of Ferroelectricity

Raman tests were conducted on the growing 2D $CuCrSe_2$ nanosheets. Figure 4a shows the schematic diagram of the Raman test. The Raman spectra of different thicknesses of 2D $CuCrSe_2$ nanosheets were studied, as shown in Figure 4b. The two main characteristic peaks at 144 and 227 cm^{-1} respectively belong to the in-plane E_g and out-of-plane A_{1g} vibration modes, which are very consistent with previous studies[34, 35]. The peak of the A_{1g} vibration mode becomes smaller and wider as the thickness increases. The peaks at 108, 170, and 220 cm^{-1} are related to the F_{2g} vibration mode, which is attributed to the transfer of Cu. Figures 4c and 4d are the angle-resolved polarized Raman spectra at 144 cm^{-1} and 227 cm^{-1}, corresponding to the E and A type phonon vibration modes, respectively.

The prerequisite for the appearance of ferroelectric properties is the breakdown of inversion symmetry[36]. Second-harmonic generation (SHG) is a second-order nonlinear optical property that can only be produced by non-centrosymmetric structures[37, 38]. We used an 800 nm wavelength laser to measure SHG on $CuCrSe_2$ nanosheets. Figure 4e depicts the power-dependent SHG intensity of the grown $CuCrSe_2$ nanosheets. The samples show a huge second-harmonic intensity, and as the excitation laser power increases monotonically, this indicates that the $CuCrSe_2$ nanosheets we grew have a huge non-centrosymmetry. The second-harmonic mapping distribution is highly uniform, indicating that the entire structure has a uniform asymmetric structure (Figure 4e inset). Extracting the SHG intensity at different laser powers and plotting it on a logarithmic scale (Figure 4f). As expected, the slope calculation ≈ 1.99, close to the theoretical value 2, because the power of the SHG signal is proportional to the square of the excitation laser power[39-41]. Additionally, the same $CuCrSe_2$ samples of different thicknesses on the same calcite substrate were tested for SHG using the same 800 nm wavelength laser. It was observed that the SHG intensity gradually increased with the increase in sample thickness. This is because the thicker the material, the more obvious its non-centrosymmetry structure, and thus the second-harmonic signal intensity is also stronger. Subsequently, extracting the SHG intensity at the same power and the information of sample thickness, the fitting result slope = 1.96 is very close to the ideal value, as shown in Figures 4g and h. We used the same homogeneous thin sheets for angle-resolved second-harmonic testing to reveal the symmetry of the 2D $CuCrSe_2$ crystal. Figures 4i and j respectively show the second-harmonic intensities related to perpendicular (polarizer direction perpendicular to analyzer direction) and parallel (polarizer direction parallel to analyzer direction) polarizations, and the patterns all show a six-fold rotational symmetry. The SHG spectrum of the $CuCrSe_2$ nanosheets reveals the non-centrosymmetry structural properties, satisfying the necessary conditions for ferroelectricity.

Generally speaking, as the temperature increases, spontaneous polarization becomes unstable and the crystal structure changes from non-centrosymmetric to highly symmetric structure[42]. Therefore, the frequency doubling intensity in the 2D $CuCrSe_2$ crystal that varies with temperature can also be used to detect the ferroelectric phase transition. Figure 4k shows the normalized SHG intensity plotted as a function of temperature. The frequency doubling intensity of the 2D $CuCrSe_2$ is stable below approximately 660 K, which is attributed to the non-centrosymmetric phase with robust order. When the temperature exceeds 660 K, the SHG intensity drops sharply, indicating that the structure of $CuCrSe_2$ changes from non-centrosymmetric to centrosymmetric. Note that the SHG intensity disappears at approximately 780 K, indicating that the Curie temperature (T_C) of the $CuCrSe_2$ crystal is approximately 780 K, which is higher than that reported for other two-dimensional ferroelectrics.

The polarization of ferroelectric materials can be switched by an external electric field. At room temperature, the ordered asymmetric positions of Cu atoms in $CuCrSe_2$ make it have stable spontaneous polarization. After applying a bias voltage, the migration of Cu atoms between the two tetrahedral positions undergoes horizontal and vertical displacements, which causes switchable IP and OOP polarization polarization.

The piezoelectric response microscopy (PFM) is a powerful tool for verifying the strong ferroelectricity of low-dimensional systems. The PFM phase hysteresis loop (black) and butterfly amplitude loop (red) are shown in Figure 4l. The 180° phase switching and clear butterfly ring indicate typical ferroelectric switching behavior, confirming the robustness of ferroelectric polarization in $CuCrSe_2$ nanosheets[43]. The external electric field engineering of ferroelectric polarization domains is one of the essential characteristics of ferroelectric materials. Therefore, we observed IP and OOP ferroelectric polarization in $CuCrSe_2$ nanosheets through PFM "read and write" operations. Figures 4m and 4n show the OOP phase and amplitude "cross" images of $CuCrSe_2$ nanosheets after writing patterns using ±7 V opposite DC bias. The bright and dark areas with nearly 180° phase contrast are shown, indicating that $CuCrSe_2$ nanosheets have inherent robust ferroelectricity and polarization switching characteristics.

The grown $CuCrSe_2$ nanosheets were transferred onto the Nb:$SrTiO_3$ substrate to complete the construction of the upper and lower end devices, and P-E hysteresis tests were conducted. We performed voltage variation tests on the devices. Figure 4o shows the P-E curves under different voltages. As the voltage increases, the polarization intensity also grows, and the area enclosed by the hysteresis loop also becomes larger. This is because a higher voltage can overcome more energy barriers for the movement across domain walls, allowing more dipole moments to participate in the polarization process, thereby obtaining a higher saturation polarization value. Then, we performed temperature variation tests on the devices. As shown in Figure 4p, as the temperature rises, the P-E hysteresis loop becomes steeper, and the saturation polarization and residual polarization intensities increase. The increase in temperature causes more thermal motion within the material, so more copper ions in $CuCrSe_2$ escape from the potential well, and the polarization can respond to changes in the electric field more quickly. However, once the temperature exceeds the critical point, the orderliness of the dipole arrangement will decrease, and the material will transform from a non-centrosymmetric ferroelectric phase to a centrosymmetric nematic phase. At 523 K, a regular P-E hysteresis loop can still be observed, which is attributed to the Curie temperature of $CuCrSe_2$ reaching 780 K. The Curie temperature of 2D $CuCrSe_2$ is far beyond room temperature, and the ferroelectric devices made from it can operate normally at higher temperatures.

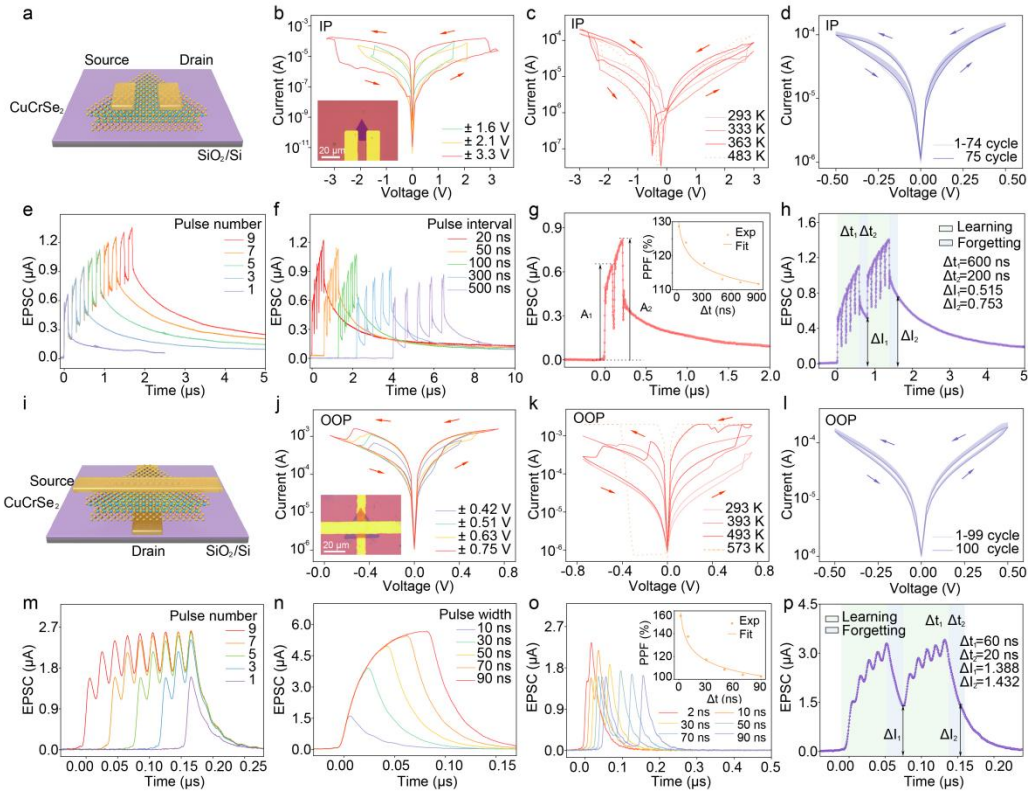

Figure 5. The memory properties and synaptic behaviors of $CuCrSe_2$-based ferroelectric devices. (a and i) The schematic of the lateral and vertical device of $CuCrSe_2$, respectively. (b and j) Sweep I-V curves at different maximum bias voltages for the lateral and vertical devices, respectively. Insets are the optical image of the lateral and vertical devices, the scale bars are 20 μm. (c and k) Temperature-dependent I-V curves for the lateral and vertical devices, respectively. (d and l) The cyclic stability tests of the lateral and vertical devices, respectively. (e and m) EPSC when 1, 3, 5, 7, and 9 electrical pulses are applied to the lateral and vertical devices, respectively. (f) The effect of different pulse intervals (i.e., pulse frequency) on the EPSC of lateral device. (n) The effect of different pulse width on the EPSC of vertical device. (g and o) Dual-pulse tests on lateral and vertical devices, respectively. (h and p) The learning-forgotten-relearning process of the lateral and vertical devices, respectively.

2.4 Artificial Synapse Devices and Neural Morphology Computing Applications

Given the superior ferroelectric properties demonstrated by $CuCrSe_2$ nanosheets, we fabricated lateral and vertical end devices based on IP and OOP polarization switching to explore their applications in non-volatile memory[44, 45]. For the lateral devices, we first transferred the 2D $CuCrSe_2$ nanosheets from the growth mica substrate to the SiO_2/Si substrate, and built two parallel Au electrodes on top as the source and drain of the device. The schematic diagram of the horizontal device is shown in Figure 5a. Then, we switched the bias voltage in the lateral direction without applying a gate voltage, obtained the output (I_{ds}-V_{ds}) curve of the device, and plotted it in logarithmic form in Figure 5b, with the OM image of the horizontal device as the illustration. It can be clearly observed that the magnetic hysteresis window of the output curve gradually expands with the increase of the maximum scanning voltage, and the current also increases accordingly. The arrows in the figure represent the voltage scanning

directions of the four processes. Moreover, we obtained a very symmetric and huge hysteresis window at ±3.3 V. The hysteresis window of the I-V curve changes with the variation of the lateral external electric field, which can be attributed to the IP ferroelectric polarization existing in the 2D $CuCrSe_2$ nanosheets, thus exhibiting the typical characteristics of ferroelectric resistors[46, 47].

Similarly, we first transferred the $CuCrSe_2$ nanosheets onto the SiO_2/Si substrate of the pre-deposited bottom Au electrode, and then transferred the top Au electrode onto it to build a vertical device with a "sandwich" layer structure. The schematic diagram of the vertical device is shown in Figure 5i. The lag of the device's output I-V curve can also be achieved by applying an external bias voltage in the vertical direction (Figure 5j). Similarly, when the maximum scanning voltage increases, the hysteresis window also increases. The illustration is the OM image of the vertical device. To eliminate the influence of stress on the material's polarization reversal, we constructed a vertical device as shown in Figure S13. Similarly, from the I-V scan curve, we can observe that the hysteresis window increases with the increase of the maximum scanning voltage, thereby excluding the influence of unnecessary stress on the material's ferroelectric polarization[48, 49]. All the above results prove that the IP and OOP ferroelectric polarizations can be switched by an external electric field, demonstrating the powerful ferroelectric resistor performance based on 2D $CuCrSe_2$.

Considering that the 2D $CuCrSe_2$ nanosheets have a Curie temperature (T_C) far exceeding room temperature (approximately 780 K), temperature-dependent I-V scanning characteristic tests were conducted on the horizontal and vertical end devices, as shown in Figures 5c and 5k respectively. The devices with both IP and OOP structures still maintained a large storage window at temperatures around 500 K, expanding their application scope in complex environments. Moreover, as the operating temperature of the devices increased, the maximum output current also gradually increased, which is a typical semiconductor characteristic. At low temperatures, copper ions are frozen in fixed positions by the $CrSe_2$ barrier, while as the temperature rises, copper ions gain sufficient energy to escape. Additionally, the cyclic stability tests of the horizontally and vertically ended memristive devices prepared were conducted, as shown in Figures 5d and 5l respectively. It was observed that even after 75 cycles (for the horizontal device) and 100 cycles (for the vertical device) of voltage cycling scans, the currents in the high-resistance state and low-resistance state remained stable, demonstrating highly repeatable hysteresis loops. This once again verifies the non-volatile memory characteristics and cyclic fatigue resistance of the devices with both polarization directions, highlighting the potential application of $CuCrSe_2$ devices in ferroelectric non-volatile devices and the promising prospects for stable information storage.

In the memristors used for neuromorphic computing, the common 2D non-volatile memory cells are composed of upper and lower electrodes and the semiconductor material within the sandwich structure layer. They can be controlled by the applied voltage to achieve the switching between high and low resistance states[50-52]. The polarization of the channel ferroelectric material can effectively enhance the separation of electron-hole pairs, increase the channel conductance, and reduce the probability of

electron-hole recombination, thereby prolonging the carrier lifetime, which becomes the key to achieving synaptic memory functions. The end devices based on $CuCrSe_2$ have the ability to detect, process and store electrical signals. In the $CuCrSe_2$ end devices, the two electrodes are respectively used as the pre-synaptic and post-synaptic, and the external electrical stimulation signal is given to the presynaptic neuron action potential, while the change in the device conductance value represents the change in synaptic weight. Even after the electrical stimulation signal stops, the device does not immediately return to its initial state, thus exhibiting typical synaptic characteristics.

Firstly, the transition from STP to LTP can be achieved by controlling the number of pulse stimulations. Figures 5e and 5m show the changes in the excitatory postsynaptic current (EPSC) when 1, 3, 5, 7, and 9 electrical pulses are applied to the horizontal and vertical devices respectively. It can be observed that after applying 1 pulse to the device, the EPSC immediately returns to its initial value. As the number of pulses increases, a higher level of current is obtained, and the current decays slowly, ultimately remaining at a relatively high current level higher than the initial state. This transition from STM to LTM can be understood as: the more times of learning, the deeper the learning is, and the slower the forgetting speed. In other words, repeated learning can make the memory deeper and the forgetting of information slower. We can also observe that when the stimulation times reach a certain level (more than 7 pulses), the current growth becomes slow. This can be attributed to the increase in synaptic weights as the biological synapse learns, but when subject to internal reinforcement constraints, in order to follow the Hebbian rule, the device's conductance will reach saturation. It can be understood that the human brain becomes tired after multiple learning sessions, and the learning efficiency decreases. Therefore, it proves that the number of pulses is one of the regulating factors of synaptic plasticity.

We also investigated the effect of different pulse intervals (i.e., pulse frequency) on the EPSC of the device. By applying five pulses with pulse intervals of 20 ns, 50 ns, 100 ns, 300 ns, and 500 ns to the horizontal device, it was observed that as the pulse interval increased, the current value decreased instead (Figure 5f). This is because the pulse period is fixed. When the pulse interval increases, it is equivalent to the pulse width decreasing and the stimulation time shortening, so the peak current value will decrease. Therefore, the memory effect decreases as the time interval between pulse stimulations increases. On the contrary, it can also be understood that as the electrical pulse frequency increases, the recombination of electrons and holes becomes more difficult. Under the same intensity and quantity of pulse stimulations, the number of electrons and holes increases with the increase in pulse frequency, resulting in a more obvious cumulative effect and a higher EPSC.

The transition from STM to LTM can also be achieved by altering the pulse width, that is, the regulation of the duty cycle (the proportion of positive voltage within the same period). We applied 10 ns, 30 ns, 50 ns, 70 ns and 90 ns pulse widths to the vertical devices, and obtained an EPSC that gradually increased with the increase in pulse width (Figure 5n). This is because when we apply a positive pulse to the device, the device is in an open state, so the larger the pulse width, the more likely the device is to be open, and its resistance value becomes smaller, thus the current value becomes larger.

Moreover, as the duration of the positive pulse increases, more traps are filled, so the current will decay more slowly.

Pairwise pulse facilitation (PPF) is a key indicator for measuring the synaptic performance of devices. Therefore, we conducted dual-pulse tests on horizontal and vertical end memristive devices. The test results are shown in Figures 5g and 5o respectively. It can be observed that as the time interval Δt between the two pulses increases, the EPSC decreases. The fitted curve of the PPF index A_2/A_1 is plotted in the insets of Figures 5g and 5o, which is in agreement with the expected results.

Based on the basic characteristics of the above synapses, we further simulated the typical human learning and memory process. By continuously applying electrical pulses to the horizontal and vertical devices, the learning-forgotten-relearning process was achieved (as shown in Figures 5h and 5p). As the electrical pulses continued to stimulate, the current of the devices increased, simulating the first learning process of the brain. After removing the electrical stimulation, the EPSC decayed to a higher level than the initial state after a period of time, reflecting that the information learned by the human brain will be partially forgotten over time. After the repeated learning or relearning process, the current value of the device increased ($\Delta I_2 > \Delta I_1$), indicating that the information learned before relearning can significantly enhance the memory ability. After experiencing two learning and memory processes, the read current of the device reached a higher level, effectively achieving the transition from STM to LTM. This demonstrates that frequent practice and reinforcement can convert STP into LTP, thereby regulating the plasticity of neuronal synapses and promoting the formation of synaptic learning and memory. Our 2D $CuCrSe_2$ devices successfully achieved the regulation of biological synaptic plasticity and simulated the human brain's learning-forgotten-memory process, demonstrating the potential in neuro-morphic computing and simulating the behavior of biological synapses.

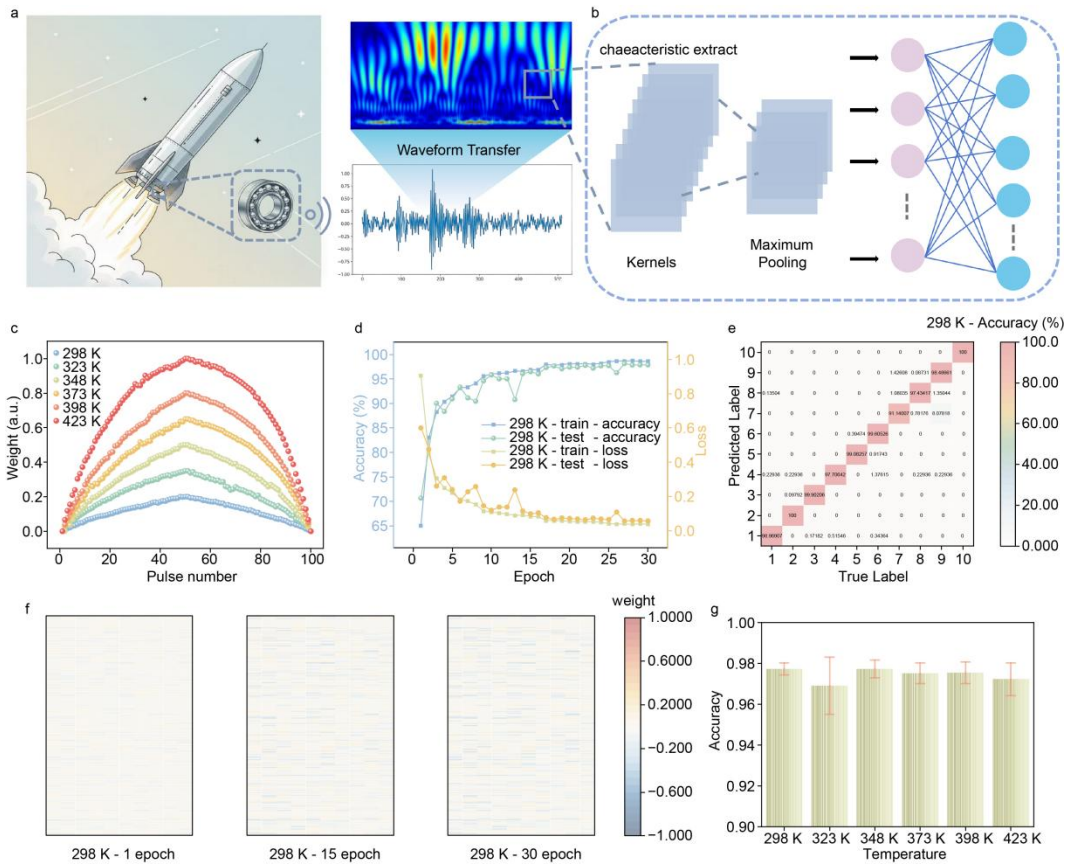

Figure 6. Neurological application. (a) The operating conditions of the bearings near the rocket engine are monitored by corresponding sensors, which then read the running status of the bearings in real time. Subsequently, wavelet transformation is applied to convert the one-dimensional signals into two-dimensional images. (b) Basic network schematic diagram: It is a CNN neural network, consisting of three convolutional layers + pooling layers + one fully connected layer + one readout layer. (c) Normalized LTP-LTD at different temperatures. (d) Network training - predicting the loss function at 298 K. (e) Classification of monitoring states under different bearing conditions at 298 K. (f) The change in the weight distribution of the last classification layer at 298 K. (g) Distribution of prediction accuracy rates at different temperatures.

Figure 6a illustrates the comprehensive evaluation workflow of the high-temperature-tolerant synaptic architecture under complex high-temperature operating environments, highlighting its potential application in aerospace materials and avionics systems. First, one-dimensional acceleration signals reflecting the real-time operating state of bearings are collected using external sensors and signal-processing units. These signals are then transformed into two-dimensional images containing time–frequency features through wavelet transformation. This conversion effectively extracts dynamic features associated with bearing operation and provides richer input information for subsequent neural-network-based recognition. As shown in Fig. 6b, the transformed feature images are fed into the neural-network model through RGB three-channel inputs and subsequently processed by multiple convolutional and pooling layers for key feature extraction and dimensionality reduction. The extracted high-dimensional features are then passed to fully connected layers to obtain the final classification results of different operating conditions. During this process, the convolutional and fully

connected layers are associated with distinct weight-matrix constraint conditions (Fig. 6c), both of which participate in the synaptic-device-based weight simulation, deployment, and updating process. Figures 6d present the evolution of the network accuracy and loss function during training, respectively. With increasing training epochs, the model accuracy gradually improves while the loss function continuously decreases, indicating effective network convergence. Under the device-constrained condition at 298 K, the model ultimately achieves a classification accuracy of approximately 98%, confirming the effectiveness of the proposed synaptic weight-mapping strategy for complex bearing fault diagnosis. Figure 6e shows the prediction results of the model for different bearing operating conditions under the device-constrained condition at 298 K, including normal operation, ball faults, outer-race faults, and inner-race faults under different frequency conditions. The confusion matrix indicates that most samples are concentrated along the diagonal, demonstrating that the model can accurately identify different operating states and exhibits robust fault-classification capability. Figure 6f illustrates the pronounced evolution of the weight matrix during training. At the initial stage, the weight distribution exhibits a relatively random pattern. After 15 training epochs, the weight matrix gradually develops distinguishable feature-distribution patterns. When the training reaches 30 epochs, the weight distribution becomes stabilized. This evolution indicates that the network can progressively extract effective features through continuous synaptic-weight modulation, ultimately enabling stable prediction performance. Figure 6g further demonstrates the stable computing capability of the synaptic device under different temperature conditions. The results show that, within the temperature range from 298 K to 423 K, the neural networks constructed using the same dataset maintain high classification accuracy, indicating that the high-temperature-tolerant synaptic architecture possesses reliable weight retention and computational robustness under thermal perturbations. The training and prediction accuracy, confusion matrices, and weight-evolution results under different temperature conditions are provided in Supplementary Figs. S22-S25. These findings further highlight the potential of the device for high-temperature avionics and intelligent health-monitoring systems.

3. Conclusion

In summary, we have successfully synthesised a novel two-dimensional ferroelectric intercalation material by the spatially confined salt-assisted CVD method. The prepared $CuCrSe_2$ nanosheets have a large domain size, high crystallization quality, superior air robustness and strong second-order nonlinear optical response. The crystal structure of Cu atoms inserted into the $CrSe_2$ interlayer was observed by STEM. The internal mechanism of its guiding extension was deeply studied, the guiding rate of $CuCrSe_2$ can change with the variation of the placement time of the substrate after peeling. The SHG signal confirmed the non-centrosymmetric structure of $CuCrSe_2$, and the Curie temperature was measured to be approximately 780 K. The ferroelectricity of IP and OOP in 2D $CuCrSe_2$ was proved by PFM. The P-E hysteresis curve exhibits the trend of changes with voltage and temperature, revealing its polarization response when subjected to external excitation variations. The $CuCrSe_2$-based two-terminal devices

achieved the basic functions of biological synapses as well as human learning-forgetting behavior. Finally, a multi-layer CNN network was established to monitor the bearing conditions near rocket launches, its recognition accuracy remained above 96% within the temperature range of 298 K to 423 K. This work not only broadens the two-dimensional P-type ferroelectric semiconductor library, but also provides a new perspective for the field of neuromorphic computing in the post-Moore era.

4. Experimental section

Growth and Transfer of 2D $CuCrSe_2$ Nanosheets:

Large-size 2D $CuCrSe_2$ nanosheets were successfully synthesized in a horizontal single-temperature zone tube furnace by a space-limited salt-assisted CVD method. Commercially available Se powder (thermo scientific, 99+%) was placed in a quartz boat in the upstream deposition zone (about 300 °C), and commercially available Cu powder (Alab Chemical Technology, 99.9%), Cr powder (Anhui Senrise Technology, 99.9%) and NaCl particles (thermo scientific, 99.99%), which were commercially available, were mixed and grinded uniformly according to the weight ratio of 10:10:1 and placed in a quartz boat in the heating center of the furnace chamber. Two freshly cleaved pieces of fluorophlogopite mica ($KMg_3AlSi_3O_{10}F_2$) were placed side by side directly above the metal powder. The nanosheets were grown in a 1-inch quartz tube under atmospheric pressure. Before heating, the chambers were air-washed twice using a mechanical pump to eliminate oxygen contamination. Subsequently, the furnace was heated to 850 ℃ within 30 minutes using 100/5 sccm of Ar/H_2 as the carrier gas and maintained at this temperature for 10 min for nanosheet growth. After the reaction, the furnace was naturally cooled to room temperature. Eventually, the grown 2D $CuCrSe_2$ nanosheets were obtained on the lower surface of mica. The grown $CuCrSe_2$ nanosheets were transferred onto the target substrates by polymethylmethacrylate (PMMA)-assisted wet transfer technique for structural characterization and device testing. The specific operation is as follows: First, spin-coat PMMA on the surface of the growth substrate and then dry it at 100 ℃ for 5 minutes. Next, immerse it in deionized water to separate it using the difference in hydrophobicity between the two. Gently lift the PMMA membrane carrying the material from the target substrate. Finally, use hot acetone vapor to remove the remaining PMMA residue on the surface.

Characterization:

The morphology and thickness of 2D $CuCrSe_2$ nanosheets were characterized by metallographic microscope (MX4R) and atomic force microscope (AFM, Oxford Instrument, MFP3D), respectively. The crystallization, phase and chemical composition of $CuCrSe_2$ nanosheets were analyzed using X-ray diffraction (XRD, Bruker AXS, D8 ADVANCE) and X-ray photoelectron spectroscopy (XPS, Thermo Fisher, ESCALAB 250Xi). Raman spectra was tested by HR-Evolution Raman system (Horiba Jobin Yvon) with an excitation laser of 532 nm. The atomic arrangement and crystal structure of $CuCrSe_2$ nanosheets were imaged by high-angle annular dark-field scanning transmission electron microscopy (HAADFSTEM, JEM ARM-200F). Second harmonic generation (SHG) characterization was carried out using an 800 nm excitation laser on the HR-Evolution Raman system, and temperature-dependent second harmonic

measurements were achieved on the heating stage. $CuCrSe_2$ nanosheets were transferred onto a double-polished conductive silicon substrate for piezoelectric force microscopy (PFM) measurements.

Device Preparation and Measurement:

The grown $CuCrSe_2$ nanosheets were first transferred from a mica substrate to a SiO_2/Si (285 nm) substrate, and then a pair of parallel Au (80 nm) electrodes were aligned above the nanosheets using a two-dimensional transfer manipulation platform to complete the horizontal device construction. For vertical devices, $CuCrSe_2$ nanosheets were first transferred to the pre-deposited bottom Au (80 nm) electrode via a transfer platform, and then, the top electrode was aligned and pressed down onto the $CuCrSe_2$ material using the same method as for horizontal devices. Electron beam lithography (EBL) and thermal vapor deposition equipment were used to pattern and pre-deposit the experimental Au electrodes, respectively. The devices were electrically tested by a digital source table (KEITHLEY 2636B).

References:

[1] Chen Xue, Chen Bingkun, Jiang Bei, et al. Nanowires for UV-vis-IR Optoelectronic Synaptic Devices [J]. Advanced Functional Materials, 2023, 33(1): 2208807.

[2] Liu Xiaoxian, Wang Shuiyuan, Di Ziye, et al. An Optoelectronic Synapse Based on Two-Dimensional Violet Phosphorus Heterostructure [J]. Advanced Science, 2023, 10(22): 2301851.

[3] Yang Hongying, Hu Yunxia, Zhang Xin, et al. Near-Infrared Optical Synapses Based on Multilayer $MoSe_2$ Moire Superlattice for Artificial Retina [J]. Advanced Functional Materials, 2024, 34(2): 2308149.

[4] Yang Ruqi, Wang Yue, Li Siqin, et al. All-Optically Controlled Artificial Synapse Based on Full Oxides for Low-Power Visible Neural Network Computing [J]. Advanced Functional Materials, 2024, 34(10): 2312444.

[5] Kumar Naveen, Patel Malkeshkumar, Thanh Tai Nguyen, et al. 2D-SnS-Embedded Schottky Device with Neurotransmitter-Like Functionality Produced Using Proximity Vapor Transfer Method for Photonic Neurocomputing [J]. Advanced Materials, 2025, 37(1): 2411420.

[6] Zhao Yukun, Cheng Linrui, Xu Rui, et al. Research progress and applications of optoelectronic synaptic devices based on 2D materials [J]. Brain-X, 2024, 2(3): e70004.

[7] Khan Asif Islam, Keshavarzi Ali, Datta Suman. The future of ferroelectric field-effect transistor technology [J]. Nature Electronics, 2020, 3(10): 588.

[8] Liu Gang, Zhang Shujun, Jiang Wenhua, et al. Losses in ferroelectric materials [J]. Materials Science & Engineering R-Reports, 2015, 89: 1.

[9] Ryu Hojoon, Xu Kai, Li Dawei, et al. Empowering 2D nanoelectronics via ferroelectricity [J]. Applied Physics Letters, 2020, 117(8): 080503.

[10] Wang Hao, Wen Yao, Zeng Hui, et al. 2D Ferroic Materials for Nonvolatile Memory Applications [J]. Advanced Materials, 2024, 37(31): 2305044.

[11] Wu Menghao, Dong Shuai, Yao Kailun, et al. Ferroelectricity in Covalently functionalized Two-dimensional Materials: Integration of High-mobility Semiconductors and Nonvolatile Memory [J]. Nano Letters, 2016, 16(11): 7309.

[12] Stengel Massimiliano, Spaldin Nicola A. Origin of the dielectric dead layer in nanoscale capacitors [J]. Nature, 2006, 443(7112): 679.

[13] Jin Tengyu, Mao Jingyu, Gao Jing, et al. Ferroelectrics-Integrated Two-Dimensional Devices toward Next-Generation Electronics [J]. ACS Nano, 2022, 16(9): 13595.

[14] Liu Fucai, You Lu, Seyler Kyle L., et al. Room-temperature ferroelectricity in $CuInP_2S_6$ ultrathin flakes [J]. Nature Communications, 2016, 7: 12357.

[15] Sharma Pankaj, Xiang Fei-Xiang, Shao Ding-Fu, et al. A room-temperature ferroelectric semimetal [J]. Science Advances, 2019, 5(7): eaax5080 .

[16] Xu Xiang, Zhong Tingting, Zuo Nian, et al. High-T_C Two-Dimensional Ferroelectric $CuCrS_2$ Grown via Chemical Vapor Deposition [J]. ACS Nano, 2022, 16(5): 8141.

[17] Ko K. T., Kim Kyoo, Kim Sung Baek, et al. RKKY Ferromagnetism with Ising-Like Spin States in Intercalated $Fe_{1/4}TaS_2$ [J]. Physical Review Letters, 2011, 107(24): 247201.

[18] Kogar A., De La Pena G. A., Lee Sangjun, et al. Observation of a Charge Density Wave Incommensuration Near the Superconducting Dome in Cu_xTiSe_2 [J]. Physical Review Letters, 2017, 118(2): 027002.

[19] Li B., Wang H., Kawakita Y., et al. Liquid-like thermal conduction in intercalated layered crystalline solids [J]. Nature Materials, 2018, 17(3): 226.

[20] Wang Mengjia, Chen Dechao, Li Zheng, et al. Epitaxial Growth of Two-Dimensional Nonlayered $AuCrS_2$ Materials via Au-Assisted Chemical Vapor Deposition [J]. Nano Letters, 2024, 24(7): 2308.

[21] Zhong Tingting, Li Xiaoyong, Wu Menghao, et al. Room-temperature multiferroicity and diversified magnetoelectric couplings in 2D materials [J]. National Science Review, 2020, 7(2): 373.

[22] Wang Ping, Zhao Yang, Na Rui, et al. Chemical Vapor Deposition Synthesis of Intrinsic High-Temperature Ferroelectric 2D $CuCrSe_2$ [J]. Advanced Materials, 2024, 36(23): 2400655.

[23] Xing Jiabao, Tang Yue, Li Jiaxin, et al. Intrinsic Out-Of-Plane and In-Plane Ferroelectricity in 2D $AgCrS_2$ with High Curie Temperature [J]. Advanced Materials, 2024, 36(50): 2407655.

[24] Zhou Yanchang, Cheng Ruiqing, Wang Hao, et al. van der Waals Epitaxial Growth of One-Unit-Cell-Thick Ferroelectric $CuCrS_2$ Nanosheets [J]. Nano Letters, 2024, 24(6): 2118.

[25] Fu W., Chai J. W., Kawai H., et al. Evidence of air-induced surface transformation of atomic step-engineered sapphire in relation to epitaxial growth of 2D semiconductors [J]. Nature Communications, 2025, 16(1): 8488.

[26] Si K. P., Zhao Y. F., Zhang P., et al. Quasi-equilibrium growth of inch-scale single-crystal monolayer α-In_2Se_3 on fluor-phlogopite [J]. Nature Communications, 2024, 15(1): 7471.

[27] Yin Lei, Cheng Ruiqing, Pan Shurong, et al. Engineering Atomic-Scale Patterning and Resistive Switching in 2D Crystals and Application in Image Processing [J]. Advanced Materials, 2023, 35(51): 2306850.

[28] Cheng Ruiqing, Yin Lei, Wen Yao, et al. Ultrathin ferrite nanosheets for room-temperature two-dimensional magnetic semiconductors [J]. Nature Communications, 2022, 13(1): 5241.

[29] Zhou Jiadong, Lin Junhao, Huang Xiangwei, et al. A library of atomically thin metal chalcogenides [J]. Nature, 2018, 556(7701): 355.

[30] Gagor A., Gnida D., Pietraszko A. Order-disorder phenomena in layered $CuCrSe_2$ crystals [J]. Materials Chemistry and Physics, 2014, 146(3): 283.

[31] Freitas Daniele C., Nunez Matias, Strobel Pierre, et al. Antiferromagnetism and ferromagnetism in layered 1T-$CrSe_2$ with V and Ti replacements [J]. Physical Review B, 2013, 87(1): 014420.

[32] Yin Lei, Cheng Ruiqing, Wen Yao, et al. High-Performance Memristors Based on Ultrathin 2D Copper Chalcogenides [J]. Advanced Materials, 2022, 34(9): 2108313.

[33] Peng Baixin, Xu Shumao, Lv Zhuoran, et al. Toward Extremely Fast Charging through Boosting Intercalative Redox Pseudocapacitance: A $SbCrSe_3$ Anode for Large and Fast Sodium Storage [J]. Advanced Energy Materials, 2023, 13(2): 2203187.

[34] Bhattacharya Shovit, Basu Ranita, Bhatt Ranu, et al. $CuCrSe_2$: a high performance phonon glass and electron crystal thermoelectric material [J]. Journal of Materials Chemistry A, 2013, 1(37): 11289.

[35] Ivanov V. G., Iliev M. N., Wang Y. H. A., et al. Ferromagnetic spinel $CuCr_2Se_4$ studied by Raman spectroscopy and lattice dynamics calculations [J]. Physical Review B, 2010, 81(22): 224302.

[36] Shi Ping-Ping, Tang Yuan-Yuan, Li Peng-Fei, et al. Symmetry breaking in molecular ferroelectrics [J]. Chemical Society Reviews, 2016, 45(14): 3811.

[37] Denev Sava A., Lummen Tom T. A., Barnes Eftihia, et al. Probing Ferroelectrics Using Optical Second Harmonic Generation [J]. Journal of the American Ceramic Society, 2011, 94(9): 2699.

[38] Zhang Jiantian, Zhao Weina, Yu Peng, et al. Second harmonic generation in 2D layered materials [J]. 2D Materials, 2020, 7(4): 042002.

[39] Wang Jing, Zhang Mingwen, Han Nannan, et al. Second Harmonic Generation in van der Waals Heterostructure of Centrosymmetric ReS_2 and Graphene [J]. Advanced Optical Materials, 2023, 11(10): 2202495.

[40] Yang Dan, Hu Xiaozong, Zhuang Minghao, et al. Inversion Symmetry Broken 2D 3R-$MoTe_2$ [J]. Advanced Functional Materials, 2018, 28(26): 1800785.

[41] Zhu Menglong, Zhong Mianzeng, Guo Xiao, et al. Efficient and Anisotropic Second Harmonic Generation in Few-Layer SnS Film [J]. Advanced Optical Materials, 2021, 9(22): 2101200.

[42] Xiao Jun, Zhu Hanyu, Wang Ying, et al. Intrinsic Two-Dimensional Ferroelectricity with Dipole Locking [J]. Physical Review Letters, 2018, 120(22): 227601.

[43] Io Weng Fu, Pang Sin Yi, Wong Lok Wing, et al. Direct observation of intrinsic room-temperature ferroelectricity in 2D layered $CuCrP_2S_6$ [J]. Nature Communications, 2023, 14(1): 7304.

[44] Saha Atanu K., Si Mengwei, Ye Peide D., et al. α-In_2Se_3 based ferroelectric-semiconductor metal junction for non-volatile memories [J]. Applied Physics Letters, 2020, 117(18): 183504.

[45] Xue Fei, He Xin, Retamal Jose Ramon Duran, et al. Gate-Tunable and Multidirection-Switchable Memristive Phenomena in a Van Der Waals Ferroelectric [J]. Advanced Materials, 2019, 31(29): 1901300.

[46] Jiang Xingan, Wang Xueyun, Wang Xiaolei, et al. Manipulation of current rectification in van der Waals ferroionic $CuInP_2S_6$ [J]. Nature Communications, 2022, 13(1): 574.

[47] Zhu Huanfeng, Li Jialin, Chen Qiang, et al. Highly Tunable Lateral Homojunction Formed in Two-Dimensional Layered $CuInP_2S_6$ via In- Plane Ionic Migration [J]. ACS Nano, 2023, 17(2): 1239.

[48] Mukherjee Subhrajit, Dutta Debopriya, Ghosh Anurag, et al. Graphene-In_2Se_3 van der Waals Heterojunction Neuristor for Optical In-Memory Bimodal Operation [J]. ACS Nano, 2023, 17(22): 22287.

[49] Zhou Yaoqiang, Tong Lei, Chen Zefeng, et al. Vertical Nonvolatile Schottky-Barrier-Field-Effect Transistor with Self-Gating Semimetal Contact [J]. Advanced Functional Materials, 2023, 33(19): 2213254.

[50] Chen Aiping, Zhang Wenrui, Dedon Liv R., et al. Couplings of Polarization with Interfacial Deep Trap and Schottky Interface Controlled Ferroelectric Memristive Switching [J]. Advanced Functional Materials, 2020, 30(43): 2000664.

[51] Higashitarumizu Naoki, Kawamoto Hayami, Lee Chien-Ju, et al. Purely in-plane ferroelectricity in monolayer SnS at room temperature [J]. Nature Communications, 2020, 11(1): 2428.

[52] Si Mengwei, Zhang Zhuocheng, Chang Sou-Chi, et al. Asymmetric Metal/α-In_2Se_3/Si Crossbar Ferroelectric Semiconductor Junction [J]. ACS Nano, 2021, 15(3): 5689.